

Room-temperature quantum sensing with photoexcited triplet electrons in organic crystals

Harpreet Singh,¹ Noella D’Souza,^{1,2} Keyuan Zhong,¹ Emanuel Druga,¹ Julianne Oshiro,³
Brian Blankenship,¹ Jeffrey A. Reimer,^{3,4} Jonathan D. Breeze,⁵ and Ashok Ajoy^{1,2,6,*}

¹Department of Chemistry, University of California, Berkeley, Berkeley, CA 94720, USA.

²Chemical Sciences Division, Lawrence Berkeley National Laboratory, Berkeley, CA 94720, USA.

³Department of Chemical and Biomolecular Engineering, University of California, Berkeley, CA 94720, USA.

⁴Materials Science Division, Lawrence Berkeley National Laboratory, Berkeley, CA 94720.

⁵Department of Physics & Astronomy, University College London, Gower Street, London, WC1E 6BT, UK.

⁶CIFAR Azrieli Global Scholars Program, 661 University Ave, Toronto, ON M5G 1M1, Canada.

Quantum sensors have notably advanced high-sensitivity magnetic field detection. Here, we report quantum sensors constructed from polarized spin-triplet electrons in photoexcited organic chromophores, specifically focusing on pentacene-doped para-terphenyl ($\approx 0.1\%$). We demonstrate essential quantum sensing properties at room temperature: electronic optical polarization and state-dependent fluorescence contrast, by leveraging differential pumping and relaxation rates between triplet and ground states. We measure high optically detected magnetic resonance (ODMR) contrast $\approx 16.8\%$ of the triplet states at room temperature, along with long coherence times under spin echo and CPMG sequences, $T_2=2.7\mu\text{s}$ and $T_2^{\text{DD}}=18.4\mu\text{s}$ respectively, limited only by the triplet lifetimes. The material offers several advantages for quantum sensing, including the ability to grow large (cm -scale) crystals at low cost, the absence of paramagnetic impurities, and the diamagnetism of electronic states used for sensing when not optically illuminated. Utilizing pentacene as a representative of a broader class of spin triplet- polarizable organic molecules, this study highlights new potential for quantum sensing in chemical systems.

Introduction – Quantum sensors [1] (q -sensors) have substantially expanded the scope for ultra-sensitive detection of magnetic fields and related parameters, e.g. temperature [2,3], pressure [4], and rotation [5–8]. Traditional q -sensors have predominantly employed semiconductor defect color centers, typified by diamond NV centers [9]. They host highly coherent electronic spins, with the ability to be optically initialized and read out at room temperature (RT). Single [10] or densely packed NV center ensembles [11] facilitate magnetometry over diverse length scales, even enabling the construction of compact, deployable magnetometry devices [12].

Recently, there has been renewed interest in q -sensors constructed from chemical systems, including molecules [13] or rare-earth ions [14,15]. The versatility of synthetic chemistry enables fabrication of tunable, atomically-defined sensor assemblies [16] at large scales. However, a critical gap remains in determining chemical systems that support coherent electronic control, optical initialization, and readout at RT, all features readily accessible with NV centers.

To address this challenge we introduce q -sensors based on photoexcited spin-triplet electrons in organic chromophore crystals. We employ pentacene doped into a para (p)-terphenyl host matrix as a model system (Fig. 1A), an important molecule in the historical context of single-molecule fluorescence [17], EPR [18–21] and room-temperature MASERs [22,23]. However, the approach here is readily applicable to a broad range of adjacent systems, including other acenes and porphyrins [24,25]. We demonstrate essential quantum sensing properties — optical initialization and readout, bright optical transitions, and coherent microwave (MW) control — under ambient conditions. This exploits differential pumping rates into the triplet state following intersystem crossing (ISC) for initialization, and varied relaxation rates of the triplet sub-levels back to the singlet ground state to produce state-dependent fluorescence contrast for readout (Fig. 1E-F). We use this to demonstrate optical detected magnetic

resonance (ODMR) of the spin transitions, with high contrast (16.8%), and long coherence times ($T_2^{\text{DD}}=18.4\mu\text{s}$) that facilitate coherent control of the molecular electronic spin at room temperature.

System and Principle – Pentacene-doped p -terphenyl single crystals from sub- μm to multiple cm -sizes (Fig. 1B) were grown using the Bridgman-Stockbarger technique [27,28] following a three-week zone refining process to purify the host material. Measurements here were conducted on a crystal with $\sim 0.1\%$ doping (Fig. 1B), focusing on a $\sim 5700\mu\text{m}^3$ spatial volume hosting $\sim 10^{11}$ molecules. Each pentacene molecule substitutes for one adjacent host counterpart, resulting in two inequivalent sites within the host lattice (at RT). The molecular coordinate axes are depicted in Fig. 1A where \hat{x} denotes the molecular long-axis (Fig. 1A); with \hat{y} and \hat{z} transverse to it, the latter being out-of-plane.

Fig. 1C illustrates the energy level structure of the π -electron, consisting of a singlet ground state $|S_0\rangle$, an excited singlet $|S_1\rangle$ of lifetime $\approx 22\text{ ns}$ [29], separated by a $\approx 2\text{ eV}$ gap and a metastable triplet state $|T_1\rangle$, with sublevels labelled $|T_{x,y,z}\rangle$. Optical excitation at 532 nm leads to fluorescence emission, and phonon-mediated ISC with high quantum efficiency $\approx 62.5\%$ [30] into an excited triplet state $|T_2\rangle$ (not shown for simplicity). The $|T_2\rangle$ electrons then rapidly undergo internal conversion (IC) into the $|T_1\rangle$ triplet state via spin-conserving non-radiative mechanisms [22]. Fig. 1D displays the RT photoluminescence (PL) spectrum under a 600nm long-pass filter; unlike cryogenic measurements [31], the zero-phonon line is not visible and PL spectrum is dominated by phonon sidebands. The photoexcited triplet spin Hamiltonian is described by $\mathcal{H}_{\text{sys}}=D\left(S_z^2-\frac{2}{3}\right)+E(S_x^2-S_y^2)$, where S is a spin-1 Pauli operator, and $D\approx 1392\text{ MHz}$ and $E\approx -53\text{ MHz}$ are the zero-field splitting parameters [21].

Fig. 1E simulates the development of triplet electronic spin polarization under pulsed laser illumination of duration $t_p=65\text{ ns}$, assuming an optical pumping rate $k_{12}=10^9\text{ s}^{-1}$, and employing population and decay rates measured previously [32,33]. $N_{x,y,z}$ refer to transient populations in the $|T_{x,y,z}\rangle$ triplet states,

* ashokaj@berkeley.edu

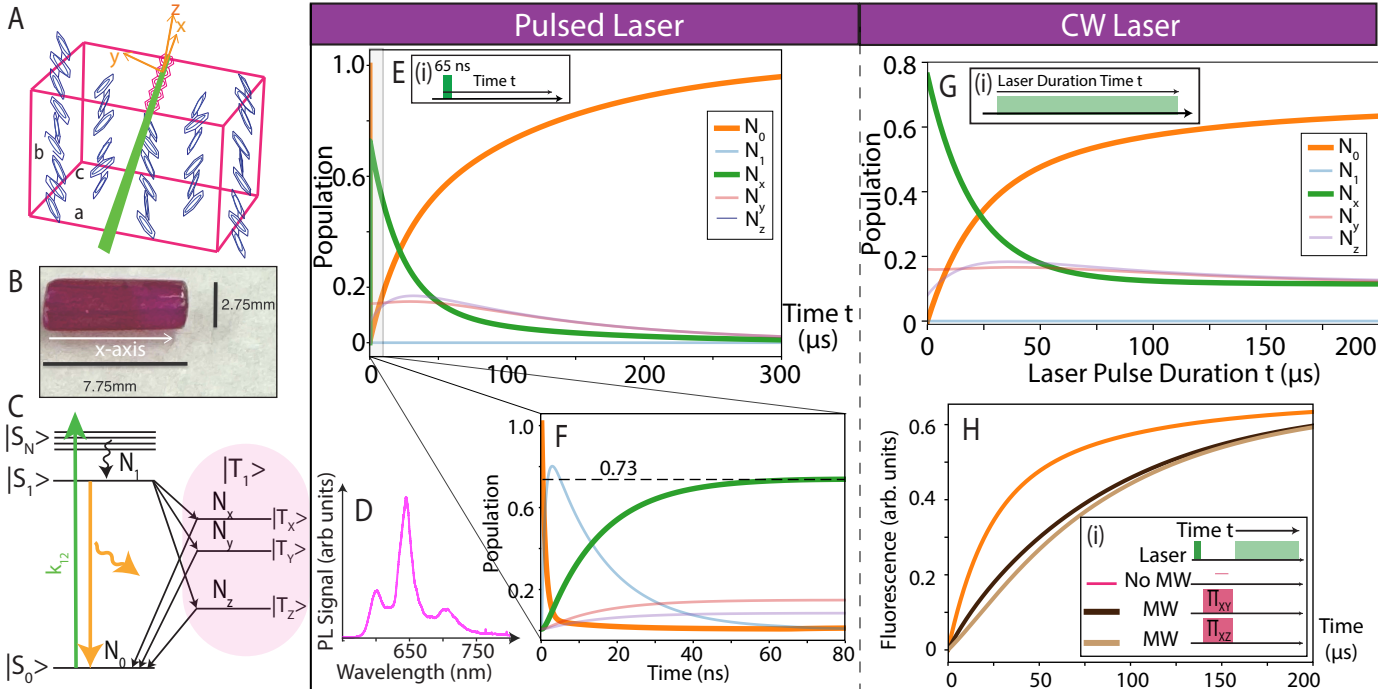


Fig. 1. **System and Principle.** (A) *Crystal structure* of pentacene molecule doped in *p*-terphenyl. Primitive lattice vectors are marked \hat{a} , \hat{b} , and \hat{c} , with lattice parameters: $a=8.2\text{\AA}$, $b=5.6\text{\AA}$, $c=13.6\text{\AA}$ [26]. Molecular axis are marked \hat{x} , \hat{y} , and \hat{z} . (B) *Photograph* of representative crystal. (C) *Energy level structure*: with marked singlet ground ($|S_0\rangle$) and excited states ($|S_1\rangle$, $|S_N\rangle$) and photoexcited triplet state $|T_1\rangle$. (D) *PL spectrum* at RT taken with a 600 nm long pass filter. (E-F) *Initialization under pulsed laser*. Simulation of triplet sublevel populations after a 65ns 532nm pulse (Inset (i)) using a pumping rate of $k_{12}=10^9\text{ s}^{-1}$. Ground singlet and $|T_x\rangle$ populations (N_0 and N_x) are highlighted. (F) Zoom in to a 80ns window shows development of transient polarization in $|T_x\rangle$ of $\approx 73\%$ due to differential (ISC) rates into the triplet state. (G) *Action of cw-laser* for polarized initial state ($N_x=0.73$) in (F) using a pumping rate of $k_{12}=10^4\text{ s}^{-1}$. (H) *Tracked population of $|S_0\rangle$ state*, reflective of the fluorescence signal, shown by the orange trace for case in (G). Dark brown and light brown traces show the same instead in case where a resonant MW π -pulse is applied to the T_{xy} or T_{xz} transitions respectively. Transient spin-dependent fluorescence emerges, producing ODMR contrast.

while $N_{0,1}$ refer to those of the $|S_{0,1}\rangle$ singlet levels respectively. Polarization occurs as a result of the differential ISC rates from $|S_1\rangle \rightarrow |T_1\rangle$. This is evident in Fig. 1F, showing the first 80 ns after the pulse, wherein a triplet polarization of $N_x \approx 0.73$ is achieved. At longer times, the spin population returns to $|S_0\rangle$ (Fig. 1E).

Readout of the $|T_1\rangle$ population levels can be performed optically by measuring the fluorescence. Starting with the polarized triplet in Fig. 1F, Fig. 1G shows the triplet state sub-level population evolution under weak *cw*-532nm illumination, with rate assumed $k_{12}=10^4\text{ s}^{-1}$. The fluorescence emission rate is then proportional to singlet ground-state population N_0 , shown by the orange line in Fig. 1H. Upon application of a MW π -pulse resonantly targeting one of the triplet transitions, the transient fluorescence profile changes due to differential relaxation rates from $|T_1\rangle \rightarrow |S_0\rangle$ depending on the triplet sub-levels coupled by the MW field. The brown lines in Fig. 1H show this for the T_{xy} ($|T_x\rangle \leftrightarrow |T_y\rangle$) and T_{xz} transitions. The difference in fluorescent emission rates forms the basis of our strategy for obtaining spin-state dependent fluorescence contrast.

ODMR of the photoexcited electronic spin-triplets – Using this strategy, Fig. 2A shows the fluorescence-measured ODMR spectrum of the triplet electrons at zero field ($B_0=0\text{ mT}$). In the simplest case, indicated in the inset in Fig. 2A, the sample is continuously illuminated with a 532 nm *cw*-laser (Coherent Verdi G2, 105 mW), and PL is measured via a lock-in amplifier (SRS) referenced to an applied 1.8 kHz amplitude-modulated MW signal [35]. MWs are produced by an AWG (Tabor P9484M) and

delivered via a 3mm-diameter loop [35]. Optical detection is through a dichroic mirror (cutoff 600nm), via a 35 mm convex lens, and into an avalanche photodiode (APD) (Hamamatsu C12703). Fig. 2A displays three prominent spectral lines that correspond to the triplet transitions. Interestingly, the T_{yz} transition exhibits an inverted ODMR contrast. We rationalize that this stems from the steady-state population in $|T_z\rangle$ being slightly higher than $|T_y\rangle$ (see Fig. 1G).

The entire ODMR scan in Fig. 2A is completed in $<1\text{ min}$, reflecting the high SNR in the measurements. We estimate a $<4.6\%$ photon collection efficiency, indicating substantial potential for future SNR improvement. The exclusive use of *cw*-illumination here mirrors the simplicity found in typical quantum sensing with NV centers, but comes at the cost of reduced contrast (cf. Fig. 3B). Furthermore, the radio-frequency (RF) nature of the T_{xy} transition ($\approx 108\text{ MHz}$) at zero-field is advantageous for practical applications due to cost-effective, high power amplifiers for these frequencies.

Analyzing the lineshape of the ODMR trace in Fig. 2A, two significant features emerge. First, we note the relatively narrow linewidths $\ell \approx 7\text{ MHz}$, even considering the relatively high density of pentacene molecules in the sample. In Fig. 2B, we estimate the true MW-unbroadened ODMR linewidth ℓ_0 by measuring ℓ as a function of MW power P_{MW} , extrapolating backwards (using the saturation function $\ell(P_{\text{MW}})=\ell_0+a\sqrt{P_{\text{MW}}}$) resulting in $\ell_0=1.9\pm 0.1\text{ MHz}$. The narrow linewidth can be attributed to extremely low concentration of other paramagnetic defects in the

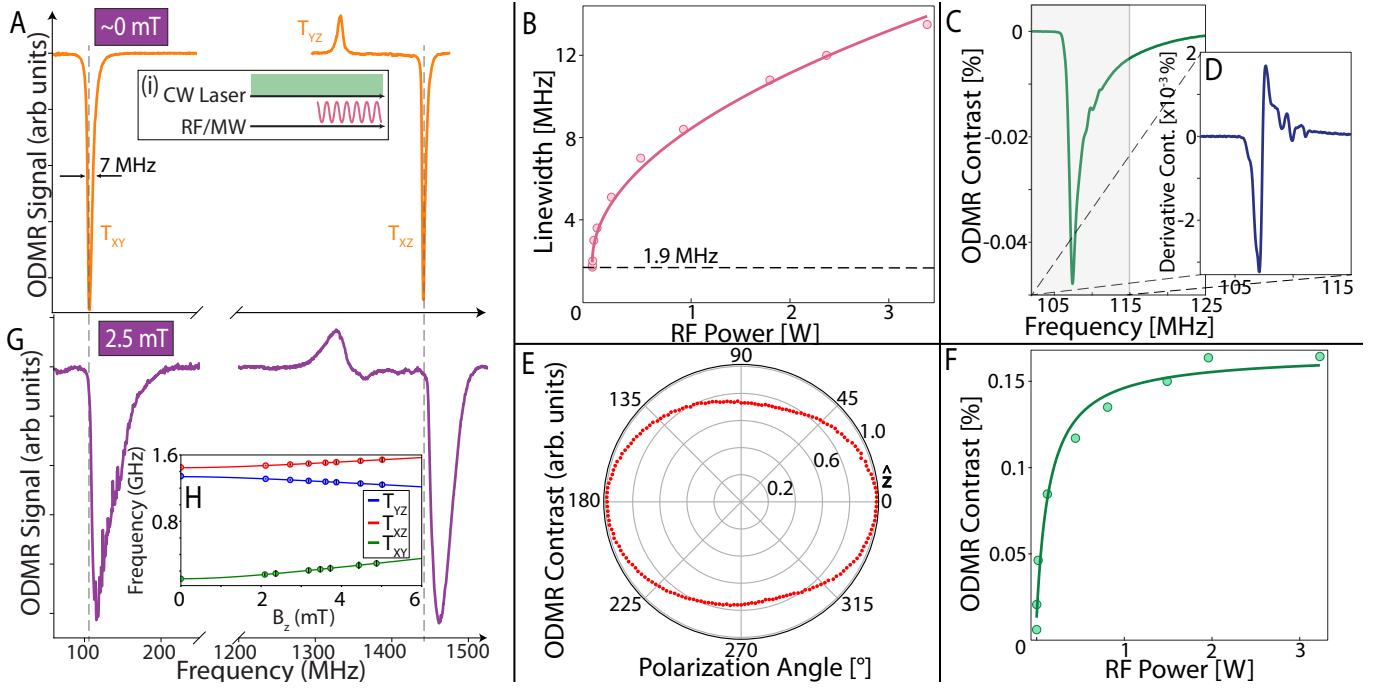


Fig. 2. **ODMR of the photoexcited triplet.** (A) ODMR spectrum at zero-field measured using cw-illumination protocol (Inset (i)) at 0.6 W MW power. Data reveals three triplet transitions at 108, 1340, and 1448 MHz; linewidth $\ell=7$ MHz. T_{yz} transition contrast is inverted in sign. (B) Linewidth dependence on MW power P_{MW} for T_{xy} transition, yielding a power unbroadened linewidth $\ell_0 \approx 1.9$ MHz. (C) Zoom in to the T_{xy} transition at low power (1.4 mW) shows asymmetric ODMR lineshape. (D) Derivative of lineshape in (C) shows spectral features related to hyperfine coupling to ^1H nuclei. (E) Excitation beam polarization of ODMR contrast, showing $\approx 27\%$ variation. (F) Contrast dependence on RF power for the T_{xy} transition. Solid line is a fit. (G) ODMR spectrum at $B_0=2.5$ mT along \hat{z} . Dashed vertical lines highlight peak shifts relative to the zero-field spectra. (H) ODMR transition frequencies with bias field B_0 along \hat{z} . Points: experimental data estimated from right spectral edges, and error bars reflecting linewidths. Solid lines: simulations.

host lattice. This contrasts with the case of diamond, where each NV center is typically associated with >10 -times as many P1 centers [36], and wherein NV-P1 interactions can significantly influence ODMR linewidths.

Second, is the notable asymmetry in the ODMR lineshapes, highlighted in the zoomed spectra in Fig. 2C, taken at low power $P_{MW}=1.45$ mW. Clear steps in the lineshape can be attributed to the hyperfine interaction with ^1H nuclei in the pentacene molecule. This asymmetry has been noted previously in EPR studies [37] but is measured here optically for the first time. Taking a derivative of the lineshape (Fig. 2D), the features become more pronounced, allowing us to identify coupling to at least three pairs of ^1H nuclei. The combination of narrow linewidth, asymmetric lineshape and a steep derivative renders the system attractive for *dc*-magnetometry applications [38,39].

Fig. 2E examines how the polarization of the excitation beam affects the ODMR contrast of the T_{xy} transition (identical results are found for other transitions). Fig. 2E displays a pronounced $\approx 27\%$ dependence on polarization angle θ . Here $\theta=0^\circ$ corresponds to light polarized along \hat{z} . We ascribe this to optimal matching of the transition dipole of the excited state. Fig. 2F highlights the dependence of the cw-illuminated ODMR contrast on MW power. As detailed below, the contrast can be significantly boosted via pulsed optical illumination (cf. Fig. 3B).

Returning to Fig. 2A and considering the action of finite magnetic field B_0 , we observe shifts in the ODMR spectra as anticipated. Fig. 2G, for example, shows the case of $\mathbf{B}_0=2.5$ mT along \hat{z} ; the shift is visible from the vertical dashed lines referencing Fig. 2A. The additional broadening here can be ascribed

to families of pentacene molecules misoriented to \mathbf{B}_0 . Points in Fig. 2H shows the measured frequencies of the three transitions as a function of $B_0 \parallel \hat{z}$ (see SI [35]), while the solid lines are the transition frequencies calculated from diagonalizing \mathcal{H}_{sys} , showing excellent agreement.

The DC sensitivity can be evaluated using the expression: $\eta_{\text{DC}} = \sigma \sqrt{\tau} / \frac{dS}{dF} \gamma_e$ [40], where $\gamma_e = 28$ MHz/mT is the gyromagnetic ratio, $\frac{dS}{dF}$, the maximal spectral slope, σ , the noise floor evaluated far-off-resonance and integration time τ chosen as the settling time of the low-pass lock-in amplifier filter. With a 2.5 mT bias field (Fig. 2G) (in the linear sensing regime, see Fig. 2H), we obtain for T_{xy} , $\eta_{\text{DC}} = 327$ nT/ $\sqrt{\text{Hz}}$ (volume normalized sensitivity $\eta_{\text{DC}}^V = 24 \mu\text{T} \mu\text{m}^{3/2} \text{Hz}^{-1/2}$) and for T_{xz} , $\eta_{\text{DC}} = 257$ nT/ $\sqrt{\text{Hz}}$ (volume normalized sensitivity $\eta_{\text{DC}}^V = 19.5 \mu\text{T} \mu\text{m}^{3/2} \text{Hz}^{-1/2}$), in spite of the low ODMR contrast (cf. Fig. 2F).

Enhanced ODMR contrast via pulsed illumination – While Fig. 2 demonstrates the simple case of cw-illumination, Fig. 1E indicates that initialization can be more efficient under pulsed optical illumination. Fig. 3A shows ODMR contrast profiles obtained for different pulse powers (for period τ_p), followed by a MW π -pulse applied to the T_{xy} transition (Fig. 3A(i)). The readout laser pulse has duration 110 μs . The optical pulses are generated by chopping the cw-beam with an Acousto-Optic Modulator (AOM) (Isomet-M1205-3). Fig. 3A demonstrates an optimal pulse period τ_p^{opt} (dashed line) that moves to shorter times with increasing optical power, yielding an increase in ODMR contrast.

Motivated by this, and to extract further contrast gains,

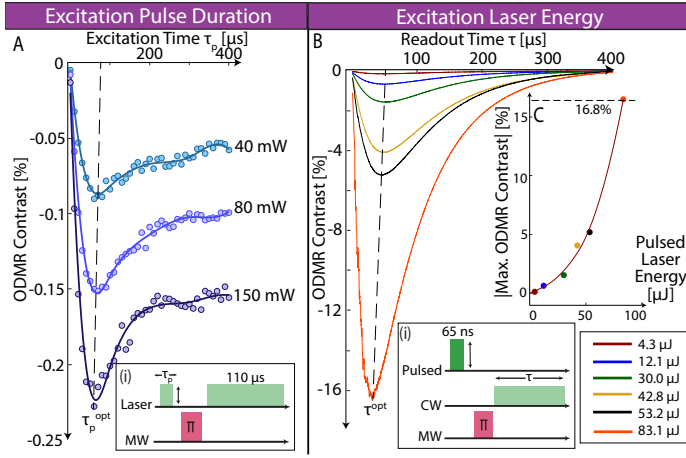


Fig. 3. **ODMR under pulsed illumination** for T_{xy} transition. (A) ODMR profiles for varying laser pulse length τ_p . Fluorescence is measured during the second $110\mu\text{s}$ *cw*-laser pulse (*Inset* (i)). Dashed line shows τ_p^{opt} , which becomes shorter with increasing power and increased contrast. (B) ODMR profiles with pulsed laser initialization (65ns), and varying periods τ of fluorescence measurement under 150mW *cw*-illumination (*Inset* (i)). Dashed line is a guide to eye to show peak shift with increasing pulsed laser energy. (C) Maximum absolute ODMR contrast with pulsed laser energy reaches $\approx 16.8\%$ at 83.1μJ. Dashed line is a guide to eye.

we employ illumination by a pulsed laser (CNI OEM-532-Q) (Fig. 3B). Fluorescence readout for τ is still performed under *cw*-illumination (150mW). Here $\tau_p=65\text{ns}$, and ODMR contrast profiles are produced for τ at different illumination powers (Fig. 3B(i)). Background subtraction is carried out by performing alternate experiments without and with the MW pulse and subtracting the result. A large contrast is observed at an optimal readout time (τ^{opt}). The origin of these profiles evident from taking the difference of the traces in Fig. 1H. Fig. 3C shows a dramatic increase of ODMR contrast at higher pulse energies, yielding 16.8% contrast at 83.1μJ. Considering simulations (Fig. 1H), we anticipate further gains at even higher energies since current experiments were limited by APD saturation beyond 80 mJ, necessitating the use of attenuating ND filters. This constraint could be circumvented by using fast MEMS optical switches [41] in future experiments to further improve contrast.

Optically-detected coherent control – Fig. 4 demonstrates coherent electronic control of the photoexcited electrons. Following the protocol in the inset, Fig. 4A displays optically detected 12.9 MHz Rabi oscillation for the driven T_{xy} transition. The observed $T_{2\rho}=135\text{ns}$ Rabi decay can be attributed to RF inhomogeneity within the driving coils.

Fig. 4B-D examines the electronic spin coherence properties in the system. Following sequences depicted in the insets, we measure T_2^* using a Ramsey scheme, T_1 through inversion recovery scheme, and T_2 using the Hahn echo sequence, yielding $T_2^*=477\pm 2\text{ns}$, $T_1=22.9\pm 0.4\mu\text{s}$, and $T_2=2.7\pm 0.1\mu\text{s}$, respectively. In the Ramsey measurements (Fig. 4B), a 20 MHz offset in the second pulse clearly distinguishes the dephasing decay. Additionally, Fig. 4E shows that employing multipulse dynamical decoupling trains can effectively prolong the T_2 coherence time yielding $T_2^{\text{DD}}=18.4\pm 0.5\mu\text{s}$ with a CPMG train spacing of 148 ns. T_2^{DD} can approach T_1 here since the latter is dominated by triplet-ground relaxation rather than spin-lattice relaxation [32].

We anticipate that shelving the population into the long-lived $|T_z\rangle$ state might allow us to overcome this limit, and access even longer coherence times.

We estimate the shot-noise limited pulsed sensitivity, $\eta_{\text{pulsed}} \approx \frac{8}{3\sqrt{3}} \frac{\hbar}{ge\mu_B} \frac{1}{C_{\text{pulsed}}\sqrt{\mathcal{N}}} \frac{\sqrt{t_I+T_2+t_R}}{T_2}$ [38], where $t_I \approx 400\mu\text{s}$ is the initialization time (including dead-time for population reset), $t_R=110\mu\text{s}$ is the window over which readout is performed (Fig. 3B), for which the time-averaged contrast is $C_{\text{pulsed}}=0.117$. \mathcal{N} denotes the photons collected per measurement and is estimated from count rate 1.9×10^{12} counts/s (PL power of $0.6\mu\text{W}$ at APD). This yields sensitivity estimates of $\eta_{\text{DC}}=0.24\text{nT Hz}^{-1/2}$ for the Ramsey sequence and $\eta_{\text{AC}}=43\text{pT Hz}^{-1/2}$ and $6.4\text{pT Hz}^{-1/2}$ for Hahn echo and CPMG sequences respectively. The corresponding volume normalized values are: Ramsey $\eta_{\text{DC}}^V=18\text{nT } \mu\text{m}^{3/2} \text{ Hz}^{-1/2}$, and $\eta_{\text{AC}}^V=3.3\text{nT } \mu\text{m}^{3/2} \text{ Hz}^{-1/2}$ and $486\text{pT } \mu\text{m}^{3/2} \text{ Hz}^{-1/2}$ for Hahn echo and CPMG respectively. We anticipate straightforward means to improve sensitivity through quantum control (exploiting the long-lived $|T_z\rangle$ state), reduction of initialization and readout times, and increasing the photon collection efficiency [42].

Discussion and Outlook – We now describe salient features of the chromophore system described here, and contrast it to conventional quantum sensors. Pentacene molecules in the host matrix act similarly to NV centers, but with higher quantum efficiency (62.5% [30] vs. 45% [43]); and since they are not associated with defect centers, every pentacene molecule can function as a quantum sensor. There are no additional paramagnetic impurities that serve as decoherence sources (for example in diamond, P1 centers [44]), allowing for quantum sensing at significantly higher electronic densities, orders of magnitude higher than NV centers. Even at $\approx 0.1\%$ doping, electronic linewidths remain narrow ($< 2\text{MHz}$), making them well-suited for bulk quantum sensing [38]. The crystals can be grown to large sizes at low costs, expanding material options for bulk magnetometry [38] and addressing the cost barriers and supply limitations of CVD/HPHT diamond manufacturing [45,46]. We note, however, that the poor thermal properties of (*p*)-terphenyl with respect to diamond [22] impose challenges in ultimately engineering large bulk magnetometer devices.

More broadly, our work suggests exciting prospects for quantum sensing using chemical systems, expanding the design space for q-sensors and their applicability. Pentacene is indicative of a wider class of systems with optically-addressable triplet electrons [24, 25, 47–49] and wherein Hamiltonian parameters like zero-field splitting can be finely tuned through chemical means [50]. Looking forward, synthetic chemistry may offer the creation of sensor arrays with precise control over spacing, topology, and concentration. One can envision molecular quantum sensor tags that integrate into various chemical and biological systems as nanoscale fluorescent magnetic field reporters [51,52].

Pentacene doped in (*p*)-terphenyl shows potential for sensing pressure [53, 54] and temperature [55]. Its more deformable lattice and lower melting point compared to NV-diamond may yield high sensitivity to small pressure and temperature changes.

Finally, the ability to hyperpolarize nuclear spins in pentacene-like systems presents opportunities [56,57]. Indeed, ^1H nuclear spins have been polarized to $> 30\%$ levels via relatively simple techniques [58,59]. A key feature is their prolonged nuclear spin-lattice relaxation time T_1 . Ref. [59,60] recorded a ^1H T_1 exceeding 100h at 100K in pentacene, attributed to the diamag-

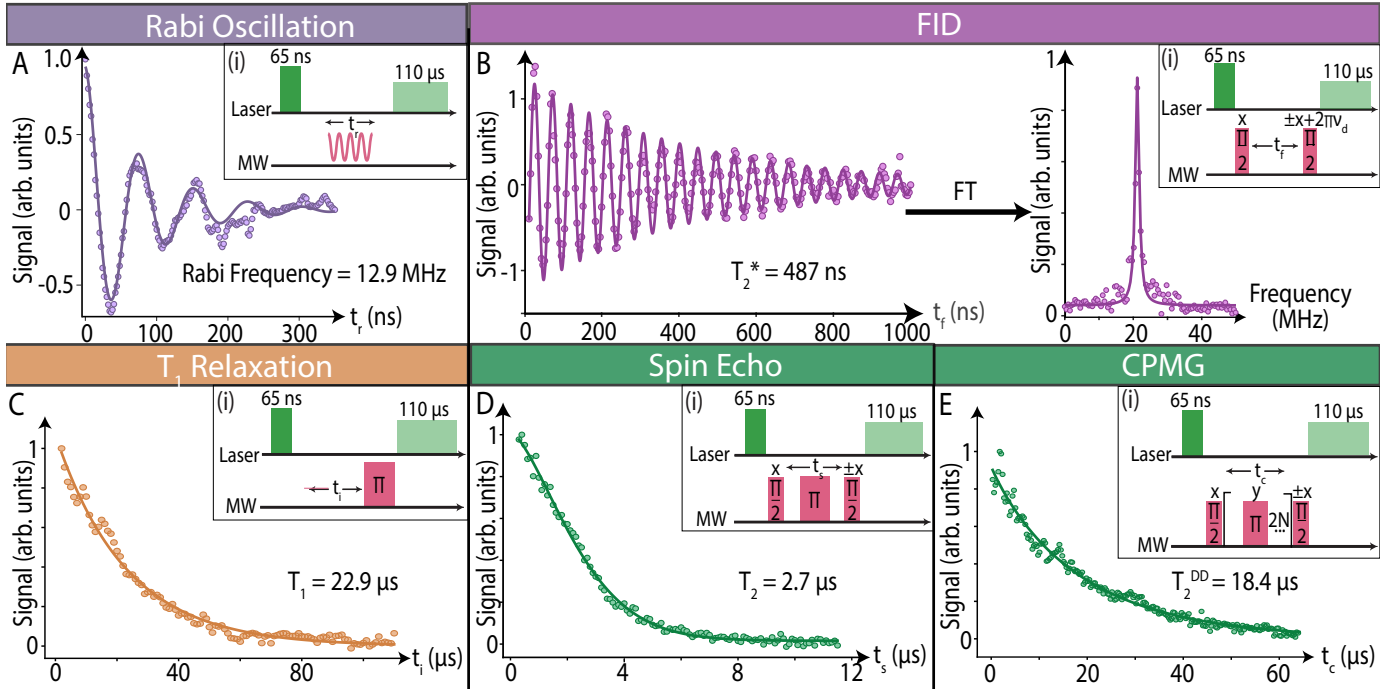


Fig. 4. **Optically-detected coherent control** of the photoexcited triplet focusing on the T_{xy} transition. (A) *Rabi oscillations* at 12.9 MHz. *Inset*: (i) Protocol used. Points are experimental data; solid line is a decaying sinusoidal fit. (B) Ramsey measurement results in $T_2^* = 487 \pm 2$ ns. Second pulse is applied with a 20 MHz (ν_d) frequency offset (*Inset* (i)). *Right panel*: Fourier transform showing peak at 20 MHz. (C) T_1 relaxation measured via inversion recovery yielding a monoexponential decay with $T_1 = 22.9 \pm 0.4 \mu\text{s}$. (D) Spin echo yields $T_2 = 2.7 \pm 0.1 \mu\text{s}$. Fit here is to a stretched exponential. (E) Multipulse dynamical decoupling using a CPMG train with interpulse spacing 148 ns, yielding a monoexponential decay $T_2^{\text{DD}} = 18.4 \pm 0.5 \mu\text{s}$. For all these relaxation measurements, each time-point signal was subtracted from the reference signal to suppress background. In the case of Rabi and T_1 experiments, reference signal for each time point repeated the same sequence without MW, while for spin-echo and CPMG experiments, the reference signal repeated the same sequence except with a π -phase added in the $\pi/2$ pulse before the $110 \mu\text{s}$ readout [34].

netic singlet ground state shielding nuclear spins from electronic relaxation. This contrasts with diamond, where ^{14}N nuclear spins exhibit short $T_1 \sim 1$ ms due to interaction with the paramagnetic NV center [7,61]. Exploiting long-lived nuclear spins opens new perspectives for gyroscopes [5,6,8], AC magnetometers [62], and fundamental condensed matter physics research

with driven, hyperpolarized, nuclei [63,64].

We gratefully acknowledge discussions with D. Suter, M. Parashar, P. Hautle, Y. Quan, J. Steiner, and funding from AFOSR (FA9550-23-1-0106), DOE BES (DE-SC0020635), NSF TAQS, DNN NNSA (FY24-LB-PD3Ta-P38), EPSRC (EP/S000798/2) and the Royal Society (URF/R1/191297). *Note added*: – When this paper was in final stages, we became aware of Ref. [65] with complementary results.

- [1] C. L. Degen, F. Reinhard, and P. Cappellaro, Quantum sensing, *Reviews of modern physics* **89**, 035002 (2017).
- [2] P. Neumann, I. Jakobi, F. Dolde, C. Burk, R. Reuter, G. Waldherr, J. Honert, T. Wolf, A. Brunner, J. H. Shim, et al., High-precision nanoscale temperature sensing using single defects in diamond, *Nano letters* **13**, 2738 (2013).
- [3] M. W. Doherty, V. M. Acosta, A. Jarmola, M. S. Barson, N. B. Manson, D. Budker, and L. C. Hollenberg, Temperature shifts of the resonances of the nv- center in diamond, *Physical Review B* **90**, 041201 (2014).
- [4] M. W. Doherty, V. V. Struzhkin, D. A. Simpson, L. P. McGuinness, Y. Meng, A. Stacey, T. J. Karle, R. J. Hemley, N. B. Manson, L. C. Hollenberg, et al., Electronic properties and metrology applications of the diamond nv- center under pressure, *Physical review letters* **112**, 047601 (2014).
- [5] A. Ajoy and P. Cappellaro, Stable three-axis nuclear-spin gyroscope in diamond, *Phys. Rev. A* **86**, 062104 (2012).
- [6] M. Ledbetter, K. Jensen, R. Fischer, A. Jarmola, and D. Budker, Gyroscopes based on nitrogen-vacancy centers in diamond, *Physical Review A* **86**, 052116 (2012).
- [7] J.-C. Jaskula, K. Saha, A. Ajoy, D. J. Twitchen, M. Markham, and P. Cappellaro, Cross-sensor feedback stabilization of an emulated quantum spin gyroscope, *Physical Review Applied* **11**, 054010 (2019).
- [8] A. Jarmola, S. Lourette, V. M. Acosta, A. G. Birdwell, P. Blümler, D. Budker, T. Ivanov, and V. S. Malinovsky, Demonstration of diamond nuclear spin gyroscope, *Science advances* **7**, eabl3840 (2021).
- [9] M. Doherty, F. Dolde, H. Fedder, F. Jelezko, J. Wrachtrup, N. Manson, and L. Hollenberg, Theory of the ground-state spin of the nv-center in diamond, *Physical Review B* **85**, 205203 (2012).
- [10] J. M. Taylor, P. Cappellaro, L. Childress, L. Jiang, D. Budker, P. R. Hemmer, A. Yacoby, R. Walsworth, and M. D. Lukin, High-sensitivity diamond magnetometer with nanoscale resolution, *Nature Phys.* **4**, 810 (2008).
- [11] L. M. Pham, D. L. Sage, P. L. Stanwix, T. K. Yeung, D. Glenn, A. Trifonov, P. Cappellaro, P. R. Hemmer, M. D. Lukin, H. Park, A. Yacoby, and R. L. Walsworth, Magnetic field imaging with nitrogen-vacancy ensembles, *New J. Phys.* **13**, 045021 (2011).
- [12] T. Wolf, P. Neumann, K. Nakamura, H. Sumiya, T. Ohshima,

- J. Isoya, and J. Wrachtrup, Subpicotesla diamond magnetometry, *Physical Review X* **5**, 041001 (2015).
- [13] M. Maylander, S. Chen, E. R. Lorenzo, M. R. Wasielewski, and S. Richert, Exploring photogenerated molecular quartet states as spin qubits and qudits, *Journal of the American Chemical Society* **143**, 7050 (2021).
- [14] S. Bayliss, D. Laorenza, P. Mintun, B. Kovos, D. Freedman, and D. Awschalom, Optically addressable molecular spins for quantum information processing, *Science* **370**, 1309 (2020).
- [15] D. Serrano, S. K. Kuppasamy, B. Heinrich, O. Fuhr, D. Hunger, M. Ruben, and P. Goldner, Ultra-narrow optical linewidths in rare-earth molecular crystals, *Nature* **603**, 241 (2022).
- [16] J. M. Zadrozny, A. T. Gallagher, T. D. Harris, and D. E. Freedman, A porous array of clock qubits, *Journal of the American Chemical Society* **139**, 7089 (2017).
- [17] W. E. Moerner and L. Kador, Optical detection and spectroscopy of single molecules in a solid, *Physical review letters* **62**, 2535 (1989).
- [18] J. Wrachtrup, C. Von Borczyskowski, J. Bernard, M. Orrit, and R. Brown, Optical detection of magnetic resonance in a single molecule, *Nature* **363**, 244 (1993).
- [19] D. J. Sloop, H.-L. Yu, T.-S. Lin, and S. Weissman, Electron spin echoes of a photoexcited triplet: Pentacene in p-terphenyl crystals, *The Journal of Chemical Physics* **75**, 3746 (1981).
- [20] H.-L. Yu, T.-S. Lin, S. Weissman, and D. J. Sloop, Time resolved studies of pentacene triplets by electron spin echo spectroscopy, *The Journal of chemical physics* **80**, 102 (1984).
- [21] T.-C. Yang, D. J. Sloop, S. Weissman, and T.-S. Lin, Zero-field magnetic resonance of the photo-excited triplet state of pentacene at room temperature, *The Journal of Chemical Physics* **113**, 11194 (2000).
- [22] M. Oxborrow, J. D. Breeze, and N. M. Alford, Room-temperature solid-state maser, *Nature* **488**, 353 (2012).
- [23] J. D. Breeze, E. Salvadori, J. Sathian, N. M. Alford, and C. W. Kay, Room-temperature cavity quantum electrodynamics with strongly coupled Dicke states, *npj Quantum Information* **3**, 1 (2017).
- [24] C. E. Tait, P. Neuhaus, H. L. Anderson, and C. R. Timmel, Triplet state delocalization in a conjugated porphyrin dimer probed by transient electron paramagnetic resonance techniques, *Journal of the American Chemical Society* **137**, 6670 (2015).
- [25] S. Richert, J. Cremers, I. Kuprov, M. D. Peeks, H. L. Anderson, and C. R. Timmel, Constructive quantum interference in a bis-copper six-porphyrin nanoring, *Nature Communications* **8**, 14842 (2017).
- [26] H. Rietveld, E. Maslen, and C. Clews, An x-ray and neutron diffraction refinement of the structure of p-terphenyl, *Acta Crystallographica Section B: Structural Crystallography and Crystal Chemistry* **26**, 693 (1970).
- [27] D. C. Stockbarger, The Production of Large Single Crystals of Lithium Fluoride, *Review of Scientific Instruments* **7**, 133 (1936), https://pubs.aip.org/aip/rsi/article-pdf/7/3/133/19250077/133_1_online.pdf.
- [28] P. W. Bridgman, Certain physical properties of single crystals of tungsten, antimony, bismuth, tellurium, cadmium, zinc, and tin, in *Papers 32-58* (Harvard University Press, 1964) pp. 1851–1932.
- [29] W. F. Koehl, B. B. Buckley, F. J. Heremans, G. Calusine, and D. D. Awschalom, Room temperature coherent control of defect spin qubits in silicon carbide, *Nature* **479**, 84 (2011).
- [30] K. Takeda, K. Takegoshi, and T. Terao, Zero-field electron spin resonance and theoretical studies of light penetration into single crystal and polycrystalline material doped with molecules photoexcitable to the triplet state via intersystem crossing, *The Journal of Chemical Physics* **117**, 4940 (2002), https://pubs.aip.org/aip/jcp/article-pdf/117/10/4940/19234643/4940_1_online.pdf.
- [31] F. Patterson, H. Lee, W. L. Wilson, and M. Fayer, Intersystem crossing from singlet states of molecular dimers and monomers in mixed molecular crystals: picosecond stimulated photon echo experiments, *Chemical Physics* **84**, 51 (1984).
- [32] H. Wu, W. Ng, S. Mirkhanov, A. Amirzhan, S. Nitnara, and M. Oxborrow, Unraveling the room-temperature spin dynamics of photoexcited pentacene in its lowest triplet state at zero field, *The Journal of Physical Chemistry C* **123**, 24275 (2019).
- [33] H. Wu, Room-temperature quantum devices based on pentacene's photo-excited triplet state in p-terphenyl, (2020).
- [34] H. Singh, A. N. Anisimov, S. S. Nagalyuk, E. N. Mokhov, P. G. Baranov, and D. Suter, Experimental characterization of spin- $\frac{3}{2}$ silicon vacancy centers in 6*h*-sic, *Phys. Rev. B* **101**, 134110 (2020).
- [35] See Supplemental Material.
- [36] C. Belthangady, N. Bar-Gill, L. M. Pham, K. Arai, D. Le Sage, P. Cappellaro, and R. L. Walsworth, Dressed-state resonant coupling between bright and dark spins in diamond, *Phys. Rev. Lett.* **110**, 157601 (2013).
- [37] T. Yago, G. Link, G. Kothe, and T.-S. Lin, Pulsed electron nuclear double resonance studies of the photoexcited triplet state of pentacene in p-terphenyl crystals at room temperature, *The Journal of chemical physics* **127** (2007).
- [38] J. F. Barry, J. M. Schloss, E. Bauch, M. J. Turner, C. A. Hart, L. M. Pham, and R. L. Walsworth, Sensitivity optimization for nv-diamond magnetometry, *Reviews of Modern Physics* **92**, 015004 (2020).
- [39] H. Wu, S. Yang, M. Oxborrow, M. Jiang, Q. Zhao, D. Budker, B. Zhang, and J. Du, Enhanced quantum sensing with room-temperature solid-state masers, *Science Advances* **8**, eade1613 (2022).
- [40] R. S. Schoenfeld and W. Harneit, Real time magnetic field sensing and imaging using a single spin in diamond, *Phys. Rev. Lett.* **106**, 030802 (2011).
- [41] *NanoSpeed™ Premium Fiber Optical Switch*, Agiltron (2024), rev. 3.
- [42] T. Wolf, P. Neumann, K. Nakamura, H. Sumiya, T. Ohshima, J. Isoya, and J. Wrachtrup, Subpicotesla diamond magnetometry, *Physical Review X* **5**, 041001 (2015).
- [43] D. Suter and F. Jelezko, Single-spin magnetic resonance in the nitrogen-vacancy center of diamond, *Progress in Nuclear Magnetic Resonance Spectroscopy* **98-99**, 50 (2017).
- [44] E. Bauch, S. Singh, J. Lee, C. A. Hart, J. M. Schloss, M. J. Turner, J. F. Barry, L. M. Pham, N. Bar-Gill, S. F. Yelin, et al., Decoherence of ensembles of nitrogen-vacancy centers in diamond, *Physical Review B* **102**, 134210 (2020).
- [45] A. Gicquel, K. Hassouni, F. Silva, and J. Achard, Cvd diamond films: from growth to applications, *Current Applied Physics* **1**, 479 (2001).
- [46] E. Pelucchi, G. Fagas, I. Aharonovich, D. Englund, E. Figueroa, Q. Gong, H. Hannes, J. Liu, C.-Y. Lu, N. Matsuda, et al., The potential and global outlook of integrated photonics for quantum technologies, *Nature Reviews Physics* **4**, 194 (2022).
- [47] M. Mayländer, O. Nolden, M. Franz, S. Chen, L. Bancroft, Y. Qiu, M. R. Wasielewski, P. Gilch, and S. Richert, Accessing the triplet state of perylene diimide by radical-enhanced intersystem crossing, *Chemical Science* **13**, 6732 (2022).
- [48] T. Hamachi, K. Nishimura, H. Kouno, Y. Kawashima, K. Tateishi, T. Uesaka, N. Kimizuka, and N. Yanai, Porphyrins as versatile, aggregation-tolerant, and biocompatible polarizing agents for triplet dynamic nuclear polarization of biomolecules, *The Journal of Physical Chemistry Letters* **12**, 2645 (2021).
- [49] K. Sakamoto, T. Hamachi, K. Miyokawa, K. Tateishi, T. Uesaka, Y. Kurashige, and N. Yanai, Polarizing agents beyond pentacene for efficient triplet dynamic nuclear polarization in glass matrices, (2023).
- [50] M. J. Amdur, K. R. Mullin, M. J. Waters, D. Puggioni, M. K. Wojnar, M. Gu, L. Sun, P. H. Oyala, J. M. Rondinelli, and D. E. Freedman, Chemical control of spin-lattice relaxation to discover a room temperature molecular qubit, *Chemical Science* **13**, 7034

- (2022).
- [51] G. Kucsko, P. Maurer, N. Y. Yao, M. Kubo, H. Noh, P. Lo, H. Park, and M. D. Lukin, Nanometre-scale thermometry in a living cell, *Nature* **500**, 54 (2013).
- [52] Y. Wu and T. Weil, Recent developments of nanodiamond quantum sensors for biological applications, *Advanced Science* **9**, 2200059 (2022).
- [53] J. Cai, F. Jelezko, and M. B. Plenio, Hybrid sensors based on colour centres in diamond and piezoactive layers, *Nature communications* **5**, 4065 (2014).
- [54] E. MacQuarrie, T. Gosavi, N. Jungwirth, S. Bhave, and G. Fuchs, Mechanical spin control of nitrogen-vacancy centers in diamond, *Physical review letters* **111**, 227602 (2013).
- [55] V. M. Acosta, E. Bauch, M. P. Ledbetter, A. Waxman, L.-S. Bouchard, and D. Budker, Temperature dependence of the nitrogen-vacancy magnetic resonance in diamond, *Phys. Rev. Lett.* **104**, 070801 (2010).
- [56] T. R. Eichhorn, B. v. d. Brandt, P. Hautle, A. Henstra, and W. T. Wenckeback, Dynamic nuclear polarisation via the integrated solid effect ii: experiments on naphthalene-h 8 doped with pentacene-d 14, *Molecular Physics* **112**, 1773 (2014).
- [57] J. Eills, D. Budker, S. Cavagnero, E. Y. Chekmenev, S. J. Elliott, S. Jannin, A. Lesage, J. Matysik, T. Meersmann, T. Prisner, *et al.*, Spin hyperpolarization in modern magnetic resonance, *Chemical Reviews* **123**, 1417 (2023).
- [58] K. Tateishi, M. Negoro, S. Nishida, A. Kagawa, Y. Morita, and M. Kitagawa, Room temperature hyperpolarization of nuclear spins in bulk, *Proceedings of the National Academy of Sciences* **111**, 7527 (2014).
- [59] T. Eichhorn, N. Niketic, B. Van Den Brandt, U. Filges, T. Panzner, E. Rantsiou, W. T. Wenckeback, and P. Hautle, Proton polarization above 70% by dnp using photo-excited triplet states, a first step towards a broadband neutron spin filter, *Nuclear Instruments and Methods in Physics Research Section A: Accelerators, Spectrometers, Detectors and Associated Equipment* **754**, 10 (2014).
- [60] Y. Quan, B. Van den Brandt, J. Kohlbrecher, and P. Hautle, Polarization analysis in small-angle neutron scattering with a transportable neutron spin filter based on polarized protons, in *Journal of Physics: Conference Series*, Vol. 1316 (IOP Publishing, 2019) p. 012010.
- [61] W. Beatrez, A. Pillai, O. Janes, D. Suter, and A. Ajoy, Electron induced nanoscale nuclear spin relaxation probed by hyperpolarization injection, *Physical Review Letters* **131**, 010802 (2023).
- [62] O. Sahin, E. de Leon Sanchez, S. Conti, A. Akkiraju, P. Reshetikhin, E. Druga, A. Aggarwal, B. Gilbert, S. Bhave, and A. Ajoy, High field magnetometry with hyperpolarized nuclear spins, *Nature communications* **13**, 5486 (2022).
- [63] W. Beatrez, C. Fleckenstein, A. Pillai, E. de Leon Sanchez, A. Akkiraju, J. Diaz Alcala, S. Conti, P. Reshetikhin, E. Druga, M. Bukov, *et al.*, Critical prethermal discrete time crystal created by two-frequency driving, *Nature Physics* **19**, 407 (2023).
- [64] K. Harkins, C. Fleckenstein, N. D'Souza, P. M. Schindler, D. Marchiori, C. Artiano, Q. Reynard-Feytis, U. Basumallick, W. Beatrez, A. Pillai, *et al.*, Nanoscale engineering and dynamical stabilization of mesoscopic spin textures, *arXiv preprint arXiv:2310.05635* (2023).
- [65] A. Mena, S. K. Mann, A. Cowley-Semple, E. Bryan, S. Heutz, D. R. McCamey, M. Attwood, and S. L. Bayliss, Room-temperature optically detected coherent control of molecular spins, *arXiv preprint arXiv:2402.07572* (2024).